Solid Immersion Maxwell's Fish-Eye Lens Without Drain

Yangyang Zhou, Zhanlei Hao, Pengfei Zhao, and Huanyang Chen*

Institute of Electromagnetics and Acoustics and Department of Physics, College of Physical Science and Technology, Xiamen University, Xiamen 361005, China

(Received 24 March 2021; revised 3 December 2021; accepted 11 February 2022; published 14 March 2022)

Maxwell's fish-eye lens (MFEL) with positive refraction has been shown to achieve perfect imaging, but with the cost of drain assistance. This has led to ongoing heated debates about the rigor of the physics of super-resolution phenomena in MFEL. In this work, we report that a MFEL embedded in an exterior coating, inspired by the solid immersion concept, can realize super-resolution imaging without a drain. Such a solution mitigates and bypasses the corresponding criticisms and debates of the past decades. We find that the total reflection at the outer solid-immersion interface and the native perfect focusing of MFEL synthetically contribute to a super-resolution image formed in the air. Moreover, this intuitive yet simple recipe can be robustly applied to other absolute instruments, such as the general Luneburg lens and more versatile superimaging systems are anticipated. We demonstrate the imaging performance in a solid immersion general Luneburg lens both numerically and experimentally, which indirectly verifies the imaging validity of the solid immersion MFEL without a drain.

DOI: 10.1103/PhysRevApplied.17.034039

I. INTRODUCTION

The diffraction limit is a fundamental issue that constrains the resolution of conventional imaging systems to within half a wavelength [1]. Supreme efforts have been made in the past few decades to overcome this limit. In 2000, Pendry proposed the concept of a perfect lens [2], which utilizes negative index materials with permittivity $\varepsilon = -1$ and permeability $\mu = -1$ (proposed by Veselago [3]) to recover all the phases of propagating waves and amplitude of evanescent waves. Initiated by the perfect lens, a series of superlenses, which project sub-diffraction-limit imaging in the near field [4,5], was demonstrated. Later, a hyperlens, which used metamaterials with hyperbolic dispersion [6,7] to convert evanescent waves to propagating waves, was proposed to achieve far-field super-resolution imaging and was manufactured by using alternate dielectric and metallic layers in a curve [8,9]. However, for both superlenses and hyperlenses, manufacturing challenges and huge intrinsic losses remained large obstacles for practical applications.

Later, Leonhardt found that the Maxwell's fish-eye lens (MFEL) [10,11], in which the active drain was put at the imaging point and a mirror was put outside boundary, could serve as a perfect lens in wave optics. Using a drain-assisted MFEL system for super-resolution imaging, electromagnetic (EM) waves at the imaging position come from both the object and a new "source"—drain—that is, the imaging is no longer an intrinsic property of the MFEL itself [12]. There were strong debates on this aspect [11–16], which aroused much attention.

The solid immersion lens (SIL) for super-resolution imaging has been extensively studied over the past few decades [17,18]. In the imaging process, the SIL utilized high-refractive-index materials to convert the evanescent waves near the object into propagating waves, and total reflection happened at the interface near the image between the lens and the air to excite evanescent waves, which improved the resolution. So far, different types of SILs have been developed from micrometer-size to nanoscale [19–21], and from conventional structures to novel metamaterial structures [22–25]. However, there are some problems owing to intrinsic aberration and chromatic aberration, which limit further applications.

In this work, we combine the solid immersion mechanism with a MFEL, by which super-resolution imaging in the MFEL without drain assistance can be achieved. In contrast to the drain-assisted MFEL, we use a truncated MFEL without a mirror, which is more accessible for application. This solution mitigates and bypasses the corresponding criticisms and debates of the past decades. Additionally, the solid immersion MFEL has advantages of both a big numerical aperture and zero aberration, thus circumventing the disadvantage of the conventional SIL, and provides more possibilities for imaging applications. We compare the positive factors of super-resolution imaging of the perfect lens, hyperlens, solid immersion MFEL, and conventional SIL (Table S2 in Supplemental Material [26]). The MFEL has advantages over other lens systems.

*kenyon@xmu.edu.cn

II. ANALYTICAL CALCULATION AND NUMERICAL SIMULATIONS OF SOLID IMMERSION MAXWELL'S FISH-EYE LENS

We analytically prove that a MFEL [10,11] can achieve super-resolution imaging with the help of a solid immersion mechanism. To verify the accuracy of the analysis, an experiment is planned to use microwaves. However, in the design process, it is very difficult to design the sample, as the refractive-index profile of the solid immersion MFEL is complex and drastically changes along the radial direction (see Sec. 4 of Supplemental Material [26]). Considering the universality of the solid immersion mechanism for realizing super-resolution imaging, we choose another absolute instrument [31], which is a class of optical devices that can realize geometrically perfect imaging, the solid immersion Luneburg lens with a gradient refractive index [32,33] to indirectly verify the super-resolution imaging of the solid immersion MFEL. The relevant experiment is carried out at microwave frequencies.

Let us start with the MFEL, which can form perfect images in geometric optics [16]. Figure 1(a) describes the refractive-index profile of the MFEL in the air and shows its ray traces from a point source. The refractive-index profile of the MFEL varies along the radial direction as follows:

$$n(r) = \begin{cases} \frac{2n_0}{1+(r/R)^2} & (0 < r < R) \\ 1 & (r \geq R) \end{cases}, \tag{1}$$

where n_0 represents the ambient refractive index, R is the radius of the MFEL and r is the distance from the center of the MFEL. To analyze the imaging performance of the MFEL in wave optics, we solve Maxwell's equations in the MFEL. For convenience, we choose cylindrical coordinates as the global coordinate system. The EM wave is assumed to be a transverse electric (TE) polarized field ($E_z, H_r,$ and H_φ). The general wave equation that governs the TE field (E_z) along the z axis can be written as

$$r^2\frac{d^2E_z}{dr^2} + r\frac{\partial E_z}{\partial r} + (k^2r^2 - m^2)E_z = 0, \tag{2}$$

where m is integer number and $k = nk_0$, in which n represents the refractive index profile and k_0 is the free-space wave vector. We introduce the wave vector $k = k_0[2n_0/1 + (r/R)^2]$ into Eq. (2) and the general solution is as follows:

$$E_z^1 = \sum_{m=-\infty}^{\infty}\left(A_m^1 r^m\left(1+r^2\right)^{(1+\sqrt{1+4k^2})/2} H_2F_1 \times\left[\frac{1+\sqrt{1+4k^2}}{2}, \frac{1+\sqrt{1+4k^2}+2m}{2}, 1+m, -r^2\right]\right)^{e^{im\theta}} \quad \text{for } 0 \leq r \leq R, \tag{3}$$

where $H_2F_1[a,b,c,z] = \sum_{m=0}^{\infty}(a^{(m)}b^{(m)}/c^{(m)})(z^m/m!)$ is hypergeometric function, A_m^1 is a complex coefficient and m is an integer. Similarly, the general solution in the air can be obtained as

$$E_z^2 = \sum_{m=-\infty}^{\infty}[B_mJ_m(k_0r) + C_mH_m(k_0r)]e^{im\theta} \text{ for } r > R, \tag{4}$$

where $J_m(k_0r)$ is the first order Bessel function and $H_m(k_0r)$ is the first order Hank function, and B_m and C_m are complex coefficients. Therefore, the whole general solution to Maxwell's equations is obtained. Similarly,

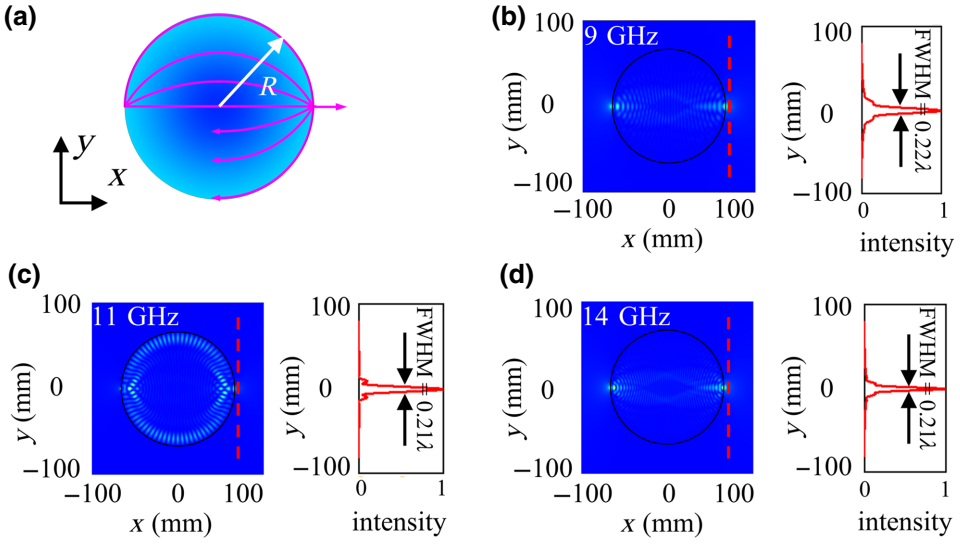

FIG. 1. Schematic of a solid immersion MFEL and its super-resolution imaging. (a) Gradient refractive-index profile and light ray trajectories in the MFEL. (b)–(d) Calculated electric field intensity distributions and the corresponding FWHMs of the solid immersion MFEL at frequencies of 9, 11, and 14 GHz respectively. The red curves represent the normalized electric field intensity along the y axis direction at the imaging point. The relative FWHMs of the imaging point are marked.

we can calculate the solution of Maxwell's equations for a transverse magnetic polarized field (H_z, E_r and E_φ). To match the results of the experiment, the TE polarized EM wave is mainly discussed in this text, as a probe serves as the experimental source and the excited filed can be regarded as a TE polarized field. Based on the above analysis, we use an addition theorem [27] to add a line current source as excitation to analytically calculate the imaging effect of the MFEL (see Sec. 1 of Supplemental Material [26]). Considering flexibility of the sample design in the microwave range, we choose an optimized MFEL with radius of 66 mm as an example. Generally, a MFEL with $n_0 = 1$ has a matching refractive index at the boundary. Evanescent waves from the object cannot be converted into propagating waves to improve resolution. To achieve super-resolution imaging, we introduce the solid immersion mechanism into MFEL. The mechanism of solid immersion MFEL's super-resolution imaging is that, (1) the EM field components with large wave vectors scattered from the object can be transferred to the boundary of the solid immersion MFEL with the help of the high refractive index as shown in Fig. S2 in Supplemental Material [26]; (2) the evanescent waves with large wave vectors are involved in imaging in the air, owing to the total reflection at the impedance mismatch between the solid immersion MFEL and the air. In this case, we choose a solid immersion MFEL with $n_0 = 2.45$. It can focus light rays emitted from a point source to another point perfectly, while a part of the light rays is reflected at the imaging point due to impedance mismatching as shown in Fig. 1(a).

Next, we numerically calculate the super-resolution imaging of the solid immersion MFEL at different frequencies. COMSOL Multiphysics software is used to make numerical simulations throughout the work. The point source is located at $x = -66$, $y = 0$ mm to excite TE cylindrical waves. Figures 1(b)–1(d) show the electric field intensity patterns and the corresponding FWHM at the frequencies of 9, 11, and 14 GHz, respectively. In the figures, the red curves show the electric field intensity and the FWHM of the imaging point is marked on the curve. Notably, the corresponding FWHM is approximate to 0.2λ at the frequencies of 9, 11, and 14 GHz, respectively, which is below the diffraction limit. Furthermore, we analytically calculate the FWHM in both x and y directions at the frequency of 14 GHz, as shown in Fig. S3 (see Supplemental Material [26]), which is entirely consistent with the simulated results. From the figure, we can see that almost half of the super-resolution imaging is in the air and that the electric field intensity at the imaging point exponentially decays along the x direction. The solid immersion MFEL successfully achieves super-resolution imaging at most frequencies. Meanwhile, for some discrete frequencies, the image quality is affected (see Fig. S6 in Supplemental Material [26]) owing to the disturbance of stable whispering-gallery modes (WGMs) [28], which are specific resonances (or modes) from continuous total internal reflection at the boundary. We also prove the adverse impacts of stable WGMs by analytical calculation (see Sec. 2 of Supplemental Material [26]).

The imaging performance of the solid immersion MFEL is investigated by varying the value of n_0 from 1 to 4 with a 0.5 step size at 11 GHz. A point source is located at $y = -66$, $x = 0$ mm to excite TE cylindrical waves. A tiny spot emerges at the opposite point in the lens and the electric field intensity patterns are plotted in Fig. S7 of Supplemental Material [26]. With increasing n_0, the evanescent wave components with large wave vector are collected at the imaging point, resulting in the improvement of resolution. The resolution of the MFEL improves with the increase of n_0. However, WGMs are inevitably excited owing to the impedance mismatch between the lens and air interface at some n_0, which damages the image quality of the solid immersion MFEL.

To further confirm the super-resolution imaging of the solid immersion MFEL, we compare the resolution of the conventional MFEL and the solid immersion MFEL with $n_0 = 2.45$ in two different ways, as shown in Fig. 2. In the first case, a point source is located at $x = -198$, $y = 0$ mm to excite TE waves at a frequency of 11 GHz. Figures 2(a) and 2(b) show the normalized electric field intensity of a row of MFELs composed of three identical lenses with $R = 66$ mm, for the conventional MFEL and solid immersion MFEL, respectively. It is noted that the resolution decreases when the imaging point is further from the source point. By comparison, we find that the solid immersion MFEL can retain super-resolution imaging even when the imaging point distance increases. This differs from the MFEL [34,35] without the super-resolution effect, in which the image quality rapidly decreases with increasing distance. The arranged solid MFELs are more effective in transmitting super-resolution information and have great potential for application in optical communication systems. Previous works have reported applications of arranged SILs [21,23]. In bioinspired artificial eyes [36], the arranged multiple lenses are used as sensors to collect information, bringing great scientific progress. In the second case, a pair of identical point sources with a spacing of 0.4λ (at a frequency of 11 GHz) are placed at the edge of the solid immersion MFEL for validation of super-resolution imaging at the frequency of 11 GHz, as depicted in Fig. 2(d). It is clearly seen that the two identical point sources are identified. In comparison, a pair of identical point sources with a spacing of 0.4λ (at a frequency of 11 GHz) are placed on the edge of the conventional MFEL. The conventional MFEL fails to identify two identical point sources, as shown in Fig. 2(c). Therefore, the super-resolution imaging of solid immersion MFEL is demonstrated.

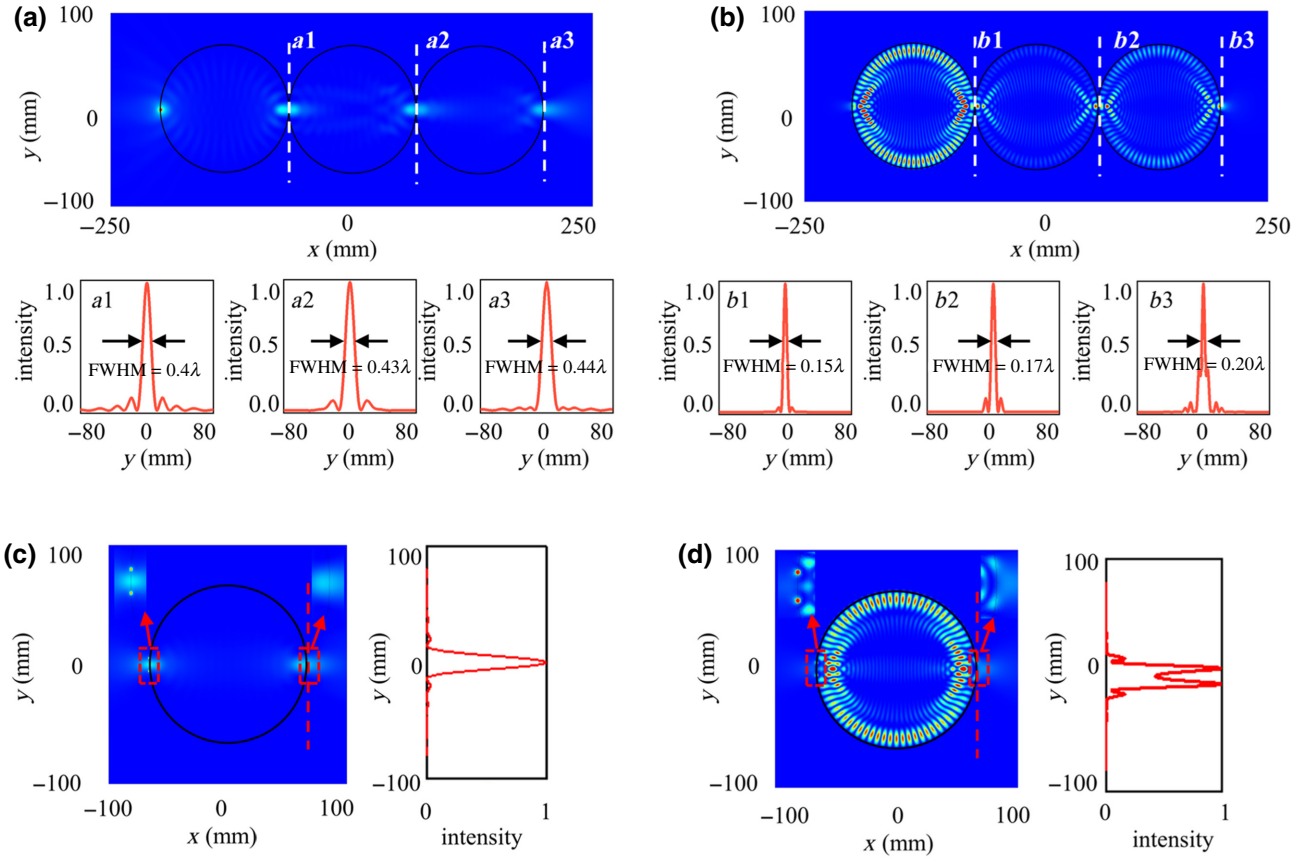

FIG. 2. Comparisons of imaging performance of the conventional MFEL and the solid immersion MFEL with $n_0 = 2.45$ at a frequency of 11 GHz. (a) The electric field intensity patterns of three interconnected identical conventional MFELs and the corresponding FWHMs at three different imaging positions $a1$, $a2$, and $a3$. (b) The electric field intensity patterns of three interconnected identical solid immersion MFELs with $n_0 = 2.45$ and the corresponding FWHM at three different imaging positions $b1$, $b2$, and $b3$. (c) Imaging performance of the conventional MFEL, of which two point sources with a spacing of 0.4λ (at frequency of 11 GHz) are placed at the edge of the lens. The conventional MFEL fails to resolve the two point sources. (d) Imaging performance of the solid immersion MFEL with $n_0 = 2.45$ in which two point sources with a spacing of 0.4λ are placed at the edge of the lens. The two points can be clearly resolved.

III. DESIGN, NUMERICAL SIMULATIONS, AND EXPERIMENTAL VALIDATION OF SOLID IMMERSION GENERAL LUNEBURG LENS

In this section, we plan to carry out the experiment to validate super-resolution imaging of the proposed solid immersion MFEL at microwave frequencies. As the refractive-index profile has a complex distribution and changes drastically in the radial direction, much effort has been made to design the sample but these attempts have failed (see Sec. 4 of Supplemental Material [26]). It is difficult to design and fabricate samples of the solid immersion MFEL. Considering the universality of the solid immersion mechanism for realizing super-resolution imaging, we use a solid immersion general Luneburg lens (GLL) (see Sec. 5 of Supplemental Material [26]) to indirectly prove the super-resolution of the solid immersion MFEL. The GLL [33] is a lens with gradient index profile $n'(r)$ [see Eq. (S17) in Supplemental Material [26]] that can form geometrically perfect imaging like the MFELs described previously and is easier to design than the MFEL, making it a good alternative to the solid immersion MFEL. We choose a GLL with a radius of $r_1 = 60$ mm, focal distance of $f_1 = f_2 = r_2 = 1.1r_1 = 66$ mm, and refractive index $n_{\mathrm{GLL}} = 2.45n'(r)$ as an example, as shown in Fig. 3(a). Full-wave numerical simulations are performed at frequencies ranging from 8 to 15 GHz to verify the super-resolution imaging performance of the solid immersion GLL. The results (see Fig. S6 in Supplemental Material [26]) show that the solid immersion GLL achieves super-resolution imaging at some discrete frequencies.

To experimentally demonstrate the super-resolution performance of the proposed solid immersion GLL, the effective medium theory [29] is utilized to design the gradient sample. According to this method, the GLL is divided into concentric rings each with the same width, which should

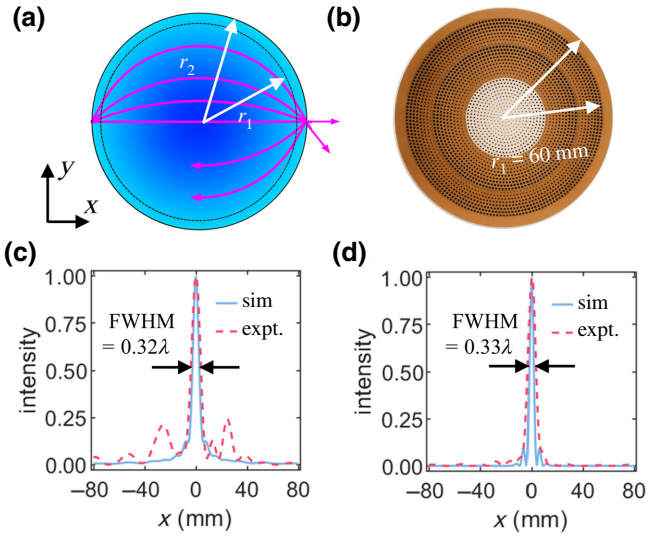

FIG. 3. Experimental measurements of super-resolution imaging. (a) Schematic of solid immersion GLL, light ray trajectories in the lens, and its gradient index profile. (b) Photograph of the fabricated solid immersion GLL. (c) and (d) Comparisons of the normalized electric field intensity profiles along the y axis from -80 to 80 mm at the imaging plane between the simulated results and experimental results at frequencies of 12 and 15 GHz, respectively. The dotted curves in red represent experimental results and the solid curves in blue represent simulated results, which show good agreement with each other.

not be more than 1/5 of the working wavelength. The concentric ring with a width of 2 mm (1/15 wavelength at the central frequency 10 GHz) is chosen. To ensure the functionality and easy fabrication, we choose the optimized sample with a radius of 66 mm and a height of 10 mm, as shown in Fig. 3(b). The sample is made from two identical lenses with a height of 5 mm by drilling different sized air holes in three dielectric plates with permittivities 20, 16, and 10.2 from the center to the boundary. Based on the effective medium theory, we calculate the effective permittivity as follows:

$$\varepsilon_{\text{eff}} = f\,\varepsilon_{\text{air}} + (1-f)\varepsilon_d, \tag{5}$$

where f is the filling fraction of the air held with a permittivity of ε_{air}, ε_d is the permittivity of the substrate dielectric plate, and ε_{eff} is the designed material permittivity. The design details of the effective refractive index and the sizes of unit cells in each layer are shown in the Figs. S14 and S15 and Table S4 of the Supplemental Material [26]. Numerical simulation results for the designed sample are shown in Fig. S16 of the Supplemental Material [26]. Next, a home-made near-field scanning field system (see Fig. S17 in the Supplemental Material [26]) is utilized to measure the electric field intensity of the solid immersion GLL. The specific testing process is depicted in Sec. 7 of the Supplemental Material [26]. Figures 3(c) and 3(d) display the simulated and measured normalized electric field intensity in the imaging plane at frequencies of 12 and 15 GHz, respectively. The experimental results are in good agreement with simulated results, which demonstrates that the sample can effectively realize super-resolution imaging. Additionally, the super-resolution effect also applies to the broadband frequencies (for more results, see Fig. S19 and Table S5 in the Supplemental Material [26]). There is a slight difference between the experimental results and the simulated results. The experimental FWHM is bigger than that of simulation due to the precision of machining and the air gap between the sample and the upper metal plate. We also discuss the focusing efficiencies [30] of the experiment and simulation and the results agree with each other, as shown in Fig. S20. From the figure, the experimental focusing efficiency can achieve over 70% at the frequencies of super-resolution imaging. It is clearly seen that the super-resolution imaging performance of the solid immersion GLL is very good in broadband frequencies. Similarly, the proposed solid immersion MFEL can overcome the diffraction limit and realize super-resolution imaging.

IV. CONCLUSION

Enlightened by SILs, we introduce the solid immersion mechanism to improve the super-resolution imaging of the MFEL and GLL without a drain, which can overcome the diffraction limit and achieve super-resolution. This mitigates and bypasses the corresponding criticisms and debates of the past decades. We fabricate a sample GLL using all-dielectric metamaterials and experimentally verify the super-resolution imaging performance of the solid immersion GLL at microwave frequencies. The effect is robust and valid for a broad band of frequencies. It provides more possibilities for overcoming the diffraction limit from microwave to optical frequencies. It is possible to pave a way for applications, such as real-time biomolecular imaging, and nanolithography. Furthermore, by combining other methods, such as transformation optics [37,38] and metasurfaces [39,40], the MFEL could be utilized to design many other kinds of super-resolution imaging systems. Although we focus here on EM waves, using the analogy of the wave equation, the basic idea of our scheme could be extended to various kinds of waves, such as acoustic [41] and elastic waves [42].

ACKNOWLEDGMENT

This research was supported by the National Key Research and Development Program of China (Grant No. 2020YFA0710100), the National Natural Science Foundation of China (Grants No. 92050102 and No. 11874311), and the Fundamental Research Funds for the Central Universities (Grant No. 20720200074). Y.Y.Z. thanks Hao

Feng for the experimental assistance and Jue Li for numerical assistance. All authors thank Professor Cheng-Wei Qiu for the helpful suggestion.

[1] Ernst Abbe, Beiträge Zur Theorie Des Mikroskops Und Der Mikroskopischen Wahrnehmung, Arch. Mikrosk. Anat. **9**, 413 (1873).
[2] J. B. Pendry, Negative Refraction Makes a Perfect Lens, Phys. Rev. Lett. **85**, 3966 (2000).
[3] V. G. Veselago, The electrodynamics of substances with simultaneously negative values of permittivity and permeability, Sov. Phys. - Usp. **10**, 509 (1968).
[4] N. Fang, H. Lee, C. Sun, and X. Zhang, Sub-Diffraction-Limited optical imaging with a silver superlens, Science **308**, 534 (2005).
[5] T. Taubner, D. Korobkin, Y. Urzhumov, G. Shvets, and R. Hillenbrand, Near-Field microscopy through a Sic superlens, Science **313**, 1595 (2006).
[6] Zubin Jacob, Leonid V. Alekseyev, and Evgenii Narimanov, Optical hyperlens: Far-field imaging beyond the diffraction limit, Opt. Express **14**, 8247 (2006).
[7] Alessandro Salandrino and Nader Engheta, Far-Field subdiffraction optical microscopy using metamaterial crystals: Theory and simulations, Phys. Rev. B **74**, 075103 (2006).
[8] Z. W. Liu, H. Lee, Y. Xiong, C. Sun, and X. Zhang, Far-Field optical hyperlens magnifying Sub-diffraction-limited objects, Science **315**, 1686 (2007).
[9] J. Rho, Z. L. Ye, Y. B. Xiong, X. Yin, Z. W. Liu, H. Choi, G. Bartal, and X. Zhang, Spherical hyperlens for two-dimensional Sub-diffractional imaging at visible frequencies, Nat. Commun. **1**, 1 (2010).
[10] J. C. Maxwell, Solution of a problem, Cambridge Dublin Math. J. **8**, 188 (1854).
[11] Ulf Leonhardt, Perfect imaging without negative refraction, New J. Phys. **11**, 093040 (2009).
[12] T. Tyc and X. Zhang, Perfect lenses in focus, Nature **480**, 42 (2011).
[13] R. J. Blaikie, Comment on 'perfect imaging without negative refraction', New J. Phys. **12**, 058001 (2010).
[14] Ulf Leonhardt, Reply to comment on 'perfect imaging without negative refraction', New J. Phys. **12**, 058002 (2010).
[15] P. Kinsler and A. Favaro, Comment on 'reply to comment on "perfect imaging without negative refraction"', New J. Phys. **13**, 028001 (2011).
[16] Ulf Leonhardt, Reply to comment on 'perfect imaging without negative refraction', New J. Phys. **13**, 028002 (2011).
[17] S. M. Mansfield and G. S. Kino, Solid immersion microscope, Appl. Phys. Lett. **57**, 2615 (1990).
[18] D. A. Fletcher, K. B. Crozier, K. W. Guarini, S. C. Minne, G. S. Kino, C. F. Quate, and K. E. Goodson, Microfabricated silicon solid immersion lens, J. Microelectromech. Syst. **10**, 450 (2001).
[19] Daniel R. Mason, Mikhail V. Jouravlev, and Kwang S. Kim, Enhanced resolution beyond the abbe diffraction limit with wavelength-scale solid immersion lenses, Opt. Lett. **35**, 2007 (2010).
[20] Myun Sik Kim, Toralf Scharf, Mohammad Tahdiul Haq, Wataru Nakagawa, and Hans Peter Herzig, Subwavelength-Size solid immersion lens, Opt. Lett. **36**, 3930 (2011).
[21] Wen Fan, Bing Yan, Zengbo Wang, and Limin Wu, Three-dimensional all-dielectric metamaterial solid immersion lens for subwavelength imaging at visible frequencies, Sci. Adv. **2**, e1600901 (2016).
[22] Z. Wang, W. Guo, L. Li, B. Luk'yanchuk, A. Khan, Z. Liu, Z. Chen, and M. Hong, Optical virtual imaging at 50 Nm lateral resolution with a white-light nanoscope, Nat. Commun. **2**, 218 (2011).
[23] R. Ahmed, A. K. Yetisen, and H. Butt, High numerical aperture hexagonal stacked ring-based bidirectional flexible polymer microlens array, ACS Nano **11**, 3155 (2017).
[24] W. X. Jiang, C. W. Qiu, T. C. Han, Q. Cheng, H. F. Ma, S. Zhang, and T. J. Cui, Broadband all-dielectric magnifying lens for far-field high-resolution imaging, Adv. Mater. **25**, 6963 (2013).
[25] Lianwei Chen, Yan Zhou, Yang Li, and Minghui Hong, Microsphere enhanced optical imaging and patterning: From physics to applications, Appl. Phys. Rev. **6**, 021304 (2019).
[26] See Supplemental Material at http://link.aps.org/supplemental/10.1103/PhysRevApplied.17.034039 for the details of the derivations of analytical calculation models, sample designs, and experimental processes, which also include Refs. [27–30].
[27] JianMin Jin, *Theory and Computation of Electromagnetic Fields* (Wiley-IEEE Press, Hoboken, New Jersey, 2010).
[28] Lu Wang, Xuefei Zhou, Shuo Yang, Gaoshan Huang, and Yongfeng Mei, 2D-material-integrated whispering-gallery-mode microcavity, Photonics Res. **7**, 905 (2019).
[29] Z. L. Mei, J. Bai, and T. J. Cui, Gradient index metamaterials realized by drilling hole arrays, J. Phys. D: Appl. Phys. **43**, 055404 (2010).
[30] A. Arbabi, Y. Horie, A. J. Ball, M. Bagheri, and A. Faraon, Subwavelength-thick lenses with high numerical apertures and large efficiency based on high-contrast transmitarrays,", Nat. Commun. **6**, 7069 (2015).
[31] Tomáš Tyc, Lenka Herzánová, Martin Šarbort, and Klaus Bering, Absolute instruments and perfect imaging in geometrical optics, New J. Phys. **13**, 115004 (2011).
[32] R. K. Luneburg, *Mathematical Theory of Optics* (University of California Press, Amsterdam, 1964).
[33] Gleb Beliakov, Numerical evaluation of the luneburg integral and Ray tracing, Appl. Opt. **35**, 1011 (1996).
[34] Si Cen Tao, Yang Yang Zhou, and Huan Yang Chen, Maxwell's fish-Eye lenses under schwartz-christoffel mappings, Phys. Rev. A **99**, 013837 (2019).
[35] X. Y. Wang, H. Y. Chen, H. Liu, L. Xu, C. Sheng, and S. N. Zhu, Self-Focusing and the Talbot Effect in Conformal Transformation Optics, Phys. Rev. Lett. **119**, 033902 (2017).
[36] Gil Ju Lee, Changsoon Choi, Dae-Hyeong Kim, and Young Min Song, Bioinspired artificial eyes: Optic components, digital cameras, and visual prostheses, Adv. Funct. Mater. **28**, 1705202 (2017).
[37] J. B. Pendry, D. Schurig, and D. R. Smith, Controlling electromagnetic fields, Science **321**, 1780 (2006).
[38] Ulf Leonhardt, Optical conformal mapping, Science **312**, 1777 (2006).

[39] Nanfang Yu, Patrice Genevet, Mikhail A. Kats, Francesco Aieta, Jean-Philippe Tetienne, Federico Capasso, and Zeno Gaburro, Light propagation with phase discontinuities: Generalized laws of reflection and refraction, Science **334**, 333 (2011).

[40] S. Sun, Q. He, S. Xiao, Q. Xu, X. Li, and L. Zhou, Gradient-index meta-surfaces as a bridge linking propagating waves and surface waves, Nat. Mater. **11**, 426 (2012).

[41] B. Yuan, Y. Tian, Y. Cheng, and X. Liu, An acoustic Maxwell's fish-eye lens based on gradient-index metamaterials, Chin. Phys. B **25**, 104301 (2016).

[42] D. Lee, Y. Hao, J. Park, I. S. Kang, S.-H. Kim, J. Li, and J. Rho, Singular Lenses for Flexural Waves on Elastic Thin Curved Plates, Phys. Rev. Appl. **15**, 034039 (2021).